

Unveiling the in-plane anisotropic dielectric waveguide modes in α-MoO_3 flakes

Ying Liao(廖莹) and Jianing Chen(陈佳宁)

Citation: Chin. Phys. B, 2024, 33 (**7**): 078401. DOI: 10.1088/1674-1056/ad3dd7
Journal homepage: http://cpb.iphy.ac.cn; http://iopscience.iop.org/cpb

What follows is a list of articles you may be interested in

Tunable superconducting resonators via on-chip control of local magnetic field

Chen-Guang Wang(王晨光), Wen-Cheng Yue(岳文诚), Xuecou Tu(涂学凑), Tianyuan Chi(迟天圆), Tingting Guo(郭婷婷), Yang-Yang Lyu(吕阳阳), Sining Dong(董思宁), Chunhai Cao(曹春海), Labao Zhang(张蜡宝), Xiaoqing Jia(贾小氢), Guozhu Sun(孙国柱), Lin Kang(康琳), Jian Chen(陈健), Yong-Lei Wang(王永磊), Huabing Wang(王华兵), and Peiheng Wu(吴培亨)
Chin. Phys. B, 2024, 33 (**5**): 058402. DOI: 10.1088/1674-1056/ad2f21

A low-cost invasive microwave ablation antenna with a directional heating pattern

Zhang Wen(文章), Xian-Qi Lin(林先其), Chen-Nan Li(李晨楠), and Yu-Lu Fan(樊钰璐)
Chin. Phys. B, 2022, 31 (**3**): 038401. DOI: 10.1088/1674-1056/ac1e1b

Integrated superconducting circuit for qubit and resonator protection

Xiao-Pei Yang(杨晓沛), Zhi-Kun Han(韩志坤), Shu-Qing Song(宋树清), Wen Zheng(郑文), Dong Lan(兰栋), Xin-Sheng Tan(谭新生), and Yang Yu(于扬)
Chin. Phys. B, 2021, 30 (**7**): 078403. DOI: 10.1088/1674-1056/ac003d

Compact NbN resonators with high kinetic inductance

Xing-Yu Wei(魏兴雨), Jia-Zheng Pan(潘佳政), Ya-Peng Lu(卢亚鹏), Jun-Liang Jiang(江俊良), Zi-Shuo Li(李子硕), Sheng Lu(卢盛), Xue-Cou Tu(涂学凑), Qing-Yuan Zhao(赵清源), Xiao-Qing Jia(贾小氢), Lin Kang(康琳), Jian Chen(陈健), Chun-Hai Cao(曹春海), Hua-Bing Wang(王华兵), Wei-Wei Xu(许伟伟), Guo-Zhu Sun(孙国柱), and Pei-Heng Wu(吴培亨)
Chin. Phys. B, 2020, 29 (**12**): 128401. DOI: 10.1088/1674-1056/abc2b8

Tunable circularly-polarized turnstile-junction mode converter for high-power microwave applications

Xiao-Yu Wang(王晓玉), Yu-Wei Fan(樊玉伟), Ting Shu(舒挺), Cheng-Wei Yuan(袁成卫), Qiang Zhang(张强)
Chin. Phys. B, 2018, 27 (**6**): 068401. DOI: 10.1088/1674-1056/27/6/068401

Unveiling the in-plane anisotropic dielectric waveguide modes in α-MoO_3 flakes

Ying Liao(廖莹)[1,2] and Jianing Chen(陈佳宁)[1,2,3,†]

[1] *Beijing National Laboratory for Condensed Matter Physics, Institute of Physics, Chinese Academy of Sciences, Beijing* 100190, *China*
[2] *School of Physical Sciences, University of Chinese Academy of Sciences, Beijing* 100049, *China*
[3] *Songshan Lake Materials Laboratory, Dongguan* 523808, *China*

(Received 13 March 2024; revised manuscript received 7 April 2024; accepted manuscript online 12 April 2024)

The unique in-plane and out-of-plane anisotropy of α-MoO_3 has attracted considerable interest with regard to potential optoelectronic applications. However, most research has focused on the mid-infrared spectrum, leaving its properties and applications in the visible and near-infrared light spectrum less explored. This study advances the understanding of waveguiding properties of α-MoO_3 by near-field imaging of the waveguide modes along the [100] and [001] directions of α-MoO_3 flakes at 633 nm and 785 nm. We investigate the effects of flake thickness and documented the modes' dispersion relationships, which is crucial for tailoring the optical responses of α-MoO_3 in device applications. Our findings enhance the field of research into α-MoO_3, highlighting its utility in fabricating next-generation optoelectronic devices due to its unique optically anisotropic waveguide.

Keywords: waveguide, anisotropic materials, near-field imaging, van der Waals materials

PACS: 84.40.Az, 78.67.–n, 07.79.Fc **DOI:** 10.1088/1674-1056/ad3dd7

1. Introduction

Van der Waals (vdW) materials,[1–3] characterized by their layered structure with atoms weakly bound through van der Waals (vdW) forces, exhibit fundamental out-of-plane anisotropy.[4] This unique property allows for easy exfoliation for material preparation and endows vdW materials with exceptional physical and chemical performance, making them a prime platform for developing future integrated photonic devices.[5–7] Graphene, with its outstanding electronic,[8,9] optical[10,11] and mechanical properties,[12,13] has become one of the most well-known vdW materials.[14–18] However, its zero-bandgap structure limits its application in digital devices and high-performance photodetectors.[19] Transition metal dichalcogenides such as MoS_2[20] and WSe_2,[21] with their adjustable bandgaps,[22] extend the applications into a broader range of optoelectronic devices beyond those possible with graphene.[23] However, the high in-plane symmetry of graphene and MoS_2 leads to almost isotropic in-plane physical properties.[24] The discovery of black phosphorus (BP) marked a significant milestone, being the first vdW material with inherent in-plane anisotropy,[25,26] and sparked increased interest in anisotropic materials. In-plane anisotropic materials added the dimension of physical property manipulation, opening up a new avenue for designing unique semiconductor devices and exploring novel applications, including polarization-sensitive photodetectors,[27] digital inverters[28] and polarization-controlled molecular electronic switches.[29] However, BP is prone to chemical degradation under atmospheric conditions, which will change its optical and electrical properties, limiting further application in devices.[30]

The α-MoO_3 has emerged as a promising candidate material, exhibiting significant in-plane and out-plane anisotropic properties in the mid-infrared (MIR) range[31–33] and demonstrating high stability in atmospheric conditions, making it suitable for near polarization-sensitive[31] and chiral[34,35] applications. However, research on the optical properties of α-MoO_3 has predominantly focused on the MIR region, with limited studies on its in-plane anisotropic optical properties within the visible (VIS) and near-infrared (NIR) ranges. Owing to its wide bandgap ($\approx$ 3.4 eV),[36] α-MoO_3 presents low optical losses in the VIS and NIR ranges and exhibits minimal nonlinear optical effects,[37] rendering it an excellent candidate for component and interconnect applications in nanophotonic devices. However, the waveguide properties related to the in-plane anisotropy of α-MoO_3 in the VIS and NIR ranges have not been explored.

This study utilized scattering-type scanning near-field optical microscopy (s-SNOM) to investigate the waveguide modes excited in α-MoO_3 flakes within the VIS and NIR ranges (633 nm and 785 nm). Our near-field imaging results demonstrate that the α-MoO_3 flakes support anisotropic waveguide modes along the [100] and [001] directions. Experimental and theoretical analysis confirm that the thicker the α-MoO_3 flakes, the higher the order of waveguide mode allowed. Moreover, we have systematically investigated the dispersion relations of the TE_0 waveguide modes excited along the [100] and [001] directions of the α-MoO_3 flakes. This work addresses the gap in near-field studies of α-MoO_3 within

†Corresponding author. E-mail: jnchen@iphy.ac.cn

© 2024 Chinese Physical Society and IOP Publishing Ltd

the VIS and NIR ranges and introduces a novel material choice for VIS and NIR waveguides, broadening the area of options for future optical device engineering.

2. Structure and physical properties of α-MoO_3

As shown in Fig. 1(a), the structural composition of α-MoO_3 is characterized by its twisted layers of [MoO_6].[38] Each bilayer forms a zig-zag arrangement shared along the [001] crystal direction at the edges and a corner-shared arrangement along the [100] crystal direction with weak vdW interactions stacking along the [010] direction.[39] This arrangement forms a distinctly layered structure, where the lattice spacings differ significantly across the three axes; this leads to in-plane and out-of-plane optical anisotropy of the α-MoO_3. Figure 1(b) exhibits the refractive indices of three directions within the VIS to NIR range, using the Cauchy model and parameters from a previous study.[40] In Fig. 1(b), α-MoO_3 exhibits pronounced in-plane and out-of-plane optical anisotropy within the VIS and NIR ranges, showing its potential for applications in advanced photonic devices such as wavelength-selective filters and optical modulators.

The synthesis of bulk α-MoO_3 employed in this study was achieved through a physical vapor deposition method utilizing an open tube furnace. Thin flakes of α-MoO_3 were mechanically exfoliated from the bulk α-MoO_3. The directional growth tendency of α-MoO_3, favoring specific crystallographic axes,[37] gives rise to its noticeable rectangular morphology, as evidenced in the transmission electron microscopy (TEM) image shown in the left panel of Fig. 1(c). The enlarged image in the right panel of Fig. 1(c) reveals that the lattice spacings along [100] and [001] directions of α-MoO_3 are 0.395 nm and 0.371 nm, respectively. These results indicate that the directions of the long and short axes of α-MoO_3 correspond to the [001] and [100] orientations, respectively.[41]

Polarization-dependent Raman spectroscopy was employed to affirm the crystallographic orientation of α-MoO_3 flakes deduced via TEM. It has been previously reported that the Raman peaks at 158 cm^{-1} and 818 cm^{-1} in α-MoO_3 exhibit sensitivity to laser polarization.[33] Notably, the vibrational mode corresponding to the 158 cm^{-1} peak is associated with vibrations along the [001] direction, while the 818 cm^{-1} peak resonates with vibrations aligned along the [100] direction. In the left panel of Fig. 1(d), the orientation angle γ, indicating the polarization direction of the incident light and the longitudinal axis of α-MoO_3, was varied to discern its impact on the Raman spectra. The right panel of Fig. 1(d) displays the polarized Raman spectra of α-MoO_3, where the intensity of the 158 cm^{-1} peak increases and that of the 818 cm^{-1} peak decreases as the angle γ decreases. This behavior highlights the alignment of the long axis of the α-MoO_3 flakes with the [001] direction and the short axis with the [100] direction. Consequently, the correlation of TEM analyses with polarization-dependent Raman spectroscopy confirms crystallographic directions of [001] and [100] of α-MoO_3 for the long and short axes, respectively.

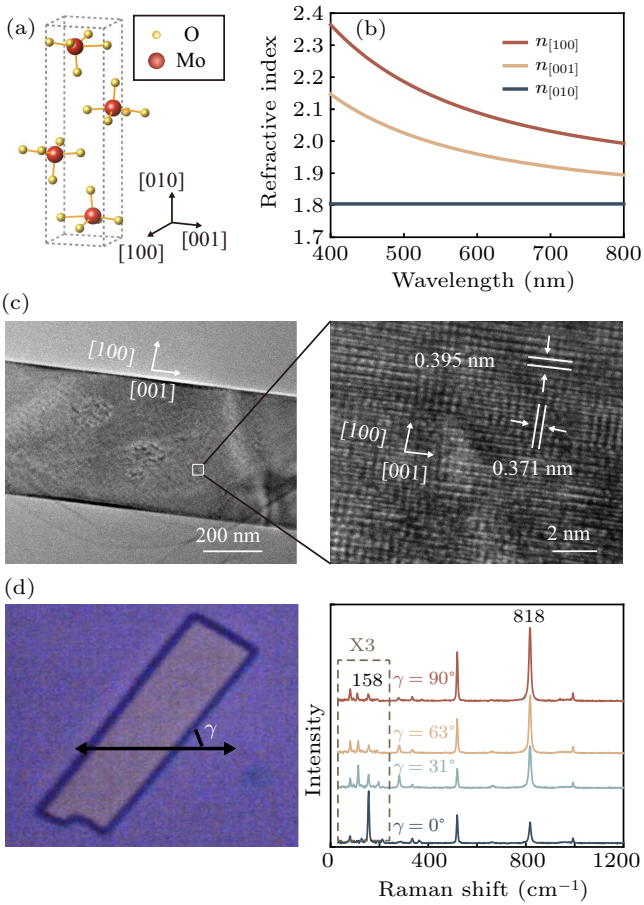


Fig. 1. The properties of α-MoO_3. (a) The crystal structure of α-MoO_3. (b) The refractive indices of α-MoO_3 in [100], [001] and [010] directions in the VIS to NIR range. (c) Left panel: TEM image of an α-MoO_3 flake. Right panel: an enlarged examination of the area delineated by the rectangle in the left panel. (d) Left panel: optical image of an α-MoO_3 flake, where the bidirectional black arrow indicates the polarization direction of the laser. γ is the angle between the polarization direction of the laser and the long-axis direction of the α-MoO_3. Right panel: the result of polarized Raman spectroscopy under 532 nm laser excitation.

3. Near-field imaging of α-MoO_3 flakes

The primary interference pathway for optical waveguide modes with a relatively small effective refractive index n_{eff} is tip excitation and boundary scattering, as illustrated in Fig. 2(a).[4,42,43] A top-down view is provided in an inset to Fig. 2(a) to illustrate the interference pathways better. Specifically, the incident light (k_{in}) is focused on the tip by a parabolic mirror. A portion of the tip-scattered light ($k_{\text{sca,tip}}$) is back-scattered into free space. However, due to the restricted collection angle of the parabolic mirror (numerical aperture = 0.37), only the scattered light with wave vectors parallel to the incident light can be effectively collected. The tip-focused light excites the waveguide mode (k_{w}) propagating to the sample

boundary and is scattered back into free space ($k_{\mathrm{sca,edge}}$) by the boundary. The scattered light from the tip ($k_{\mathrm{sca,tip}}$) and the boundary ($k_{\mathrm{sca,edge}}$) interferes coherently to form interference fringes. The periodicity of these fringes exhibits a significant directional dependence on α and β in Fig. 2(a). α is the angle between the incident light and the sample plane, which is 40° in our s-SNOM. β is the angle between the in-plane component of the incident light and the sample boundary. $k_{\mathrm{in},//}$ in Fig. 2(a) is the projection of the incident light wavevector in the sample plane. The following equation can quantitatively describe this relationship:[42]

$$k_\rho/k_0 = k_{\mathrm{m}}/k_0 \cos\phi + \sin\beta\cos\alpha, \tag{1}$$

where k_{m} is the wave vector of the waveguide mode. k_ρ is defined as $2\pi/\rho$, where ρ is the period of the fringes and k_0 is the wave vector of light in free space. ϕ is the propagation angle of waveguide mode, which can be determined through the conservation of momentum along the edge direction

$$\phi = \sin^{-1}\left[\left(\frac{k_0}{k_{\mathrm{m}}}\right)\cos\alpha\cos\beta\right]. \tag{2}$$

Equation (1) describes the relationship between the fringe period and the incident angle β.

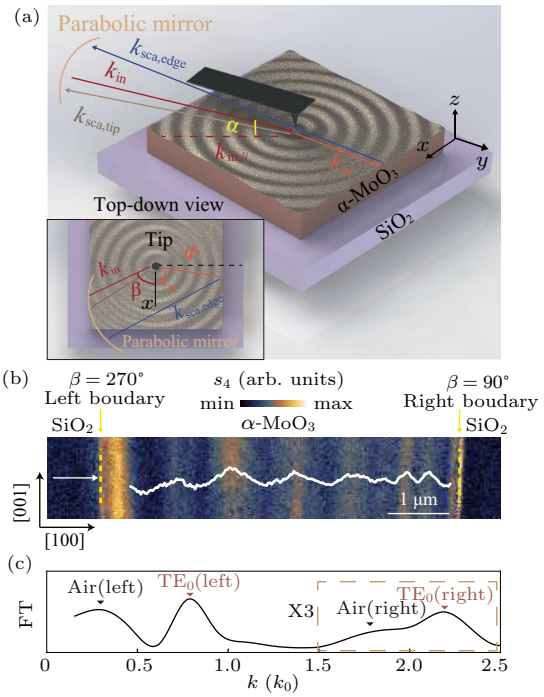


Fig. 2. The interference path of the waveguide mode on α-MoO_3 flakes. (a) Schematic diagrams of near-field imaging on α-MoO_3 by s-SNOM. The inset shows a top-down view. The *xyz*-coordinate system represents the spatial coordinates, where the *x*-axis is parallel to the sample boundary and the *z*-axis is perpendicular to the sample surface. (b) Near-field imaging of the waveguide mode propagating along the [100] direction of an α-MoO_3 flake under 785 nm incident light excitation. The white arrow indicates the direction of incident light. The yellow dashed lines indicate the boundaries of the α-MoO_3 flake. (c) Fourier transform result of the near-field amplitude curves extracted along the [100] direction from (b).

We conducted near-field experiments at room temperature and pressure using an s-SNOM from Neaspec with a Pt/Ir tip (curvature radius ~ 30 nm). The resonance frequency was 270 kHz, with an oscillation amplitude of ~ 70 nm. Figure 2(b) displays the near-field image of an α-MoO_3 flake under 785 nm incident light with perpendicular boundary incidence. At the right boundary $\beta = 90°$, and at the left boundary $\beta = 270°$. Figure 2(c) shows the Fourier transform result of Fig. 2(b). We can observe that the period of the left fringes is larger than that of the right fringes, consistent with Eq. (1). Furthermore, the fringes on the left side are brighter than those on the right. Incident light enters from left to right, and the parabolic mirror is on the left side of the sample. Therefore, the AFM tip obstructs the signal scattered from the right boundary, resulting in lower near-field intensity compared with the left boundary. In subsequent sections of this paper, near-field imaging is performed proximal to the right boundary.

Three α-MoO_3 thin flakes of varying thickness were selected to investigate the waveguide modes at different thicknesses. The AFM images in Fig. 3(a) reveal remarkably smooth and pristine surfaces in all three α-MoO_3 thin flakes. In Fig. 3(b), the line profiles extracted along the red dashed lines from Fig. 3(a) reveal the thicknesses of the three α-MoO_3 thin flakes to be 758 nm, 300 nm and 180 nm, respectively. We utilized COMSOL to analyze the dielectric waveguides of α-MoO_3 with three thicknesses (758 nm, 300 nm and 180 nm) along the [100] direction to investigate the existing waveguide modes and obtain the effective refractive index n_{eff}. The simulation results in Fig. S1 illustrate the distribution of TE and TM mode electromagnetic fields at the boundaries. The 758-nm-thick α-MoO_3 supports six waveguide modes, TE_0, TE_1, TE_2, TM_0, TM_1 and TM_2, along the [100] direction. As the thickness decreases, the number of supported waveguide modes reduces. Specifically, the 300-nm-thick α-MoO_3 supports four waveguide modes (TE_0, TE_1, TM_0 and TM_1) along the [100] direction, while the 180-nm-thick α-MoO_3 supports two waveguide modes (TM_0 and TE_0) along the [100] direction. The n_{eff} of different waveguide modes in α-MoO_3 flakes with three different thicknesses are listed in Table S1.

Maintaining a vertical ($\beta = 90°$) incidence of 785 nm light from the left boundary, we conducted near-field imaging on α-MoO_3 flakes with three different thicknesses, as shown in Fig. 3(c). The white curves in Fig. 3(c) correspond to the near-field amplitude maps extracted along the [100] direction. The observation location is near the right boundary. However, the α-MoO_3 flakes exhibit a rectangular shape with smaller dimensions along the short axis ([100] direction). Therefore, the near-field images near the right boundary are inevitably influenced by the interference fringes from the left boundary. The interference fringes from the left boundary are not included in the subsequent waveguide mode enumeration.

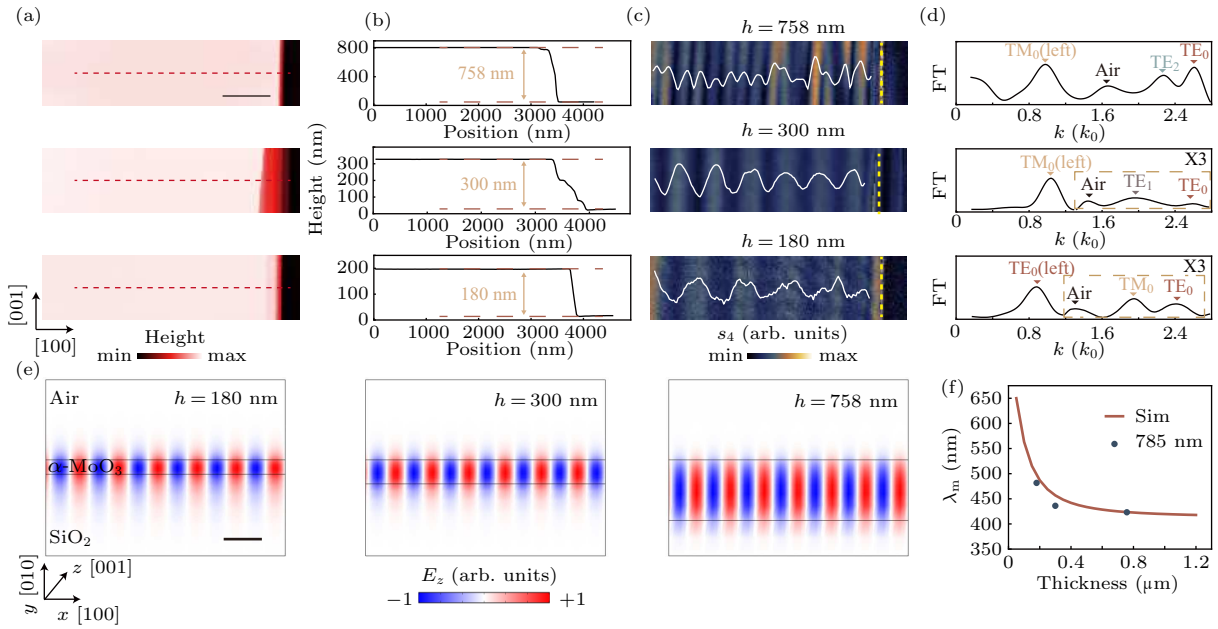


Fig. 3. Waveguide modes along the [100] direction on three α-MoO_3 flakes of different thicknesses under 785 nm incident light at 90°. (a) Atomic force microscopy images of three different thicknesses of α-MoO_3 flakes. The scale bar is 1 μm. (b) Line profiles extracted from (a) along the red dashed line. (c) Near-field imaging of the α-MoO_3 flakes with $h = 180$ nm, 300 nm and 758 nm under 785 nm incident light at 90°. The yellow dashed lines represent the right boundary of the α-MoO_3 flakes. (d) Fourier transform results for the near-field amplitude curves extracted along the [100] direction from (c). (e) TE_0 mode E_z distribution of the propagation field along the [100] direction of the α-MoO_3 flakes. The scale bar is 500 nm. (f) Experimental and simulated relationship between the α-MoO_3 thickness and the wavelength of the TE_0 mode ($\lambda_m = \lambda_0/n_{eff}$) along the [100] direction excited by 785 nm incident light.

From the near-field images of the three different thicknesses, the near-field intensity of the α-MoO_3 flakes with a thickness of 758 nm is significantly higher than that of the 300 nm and 180 nm α-MoO_3 flakes. Fourier transforms were performed separately on the extracted near-field profiles to analyze the fringe patterns accurately, resulting in curves with multiple peaks. By substituting the peak positions into Eq. (1), the corresponding q_w values were calculated. Then, the experimentally effective refractive index was determined from the equation $n_{eff} = k_w/k_0$. By comparing the simulated n_{eff} of different waveguide modes in Table S1, we can identify the waveguide modes that correspond to each peak position. The results are shown in Fig. 3(d). In Fig. 3(d), TE_0 and TE_2 modes are observed in 758-nm-thick α-MoO_3. For 300-nm-thick α-MoO_3, TE_0 and TE_1 modes are present, while the 180-nm-thick α-MoO_3 exhibits TE_0 and TM_0 modes. Our experimental results confirm that thicker α-MoO_3 flakes excite higher-order TE modes under the same incident condition. Among these three thicknesses of α-MoO_3, the TE_0 mode is observed in all cases. The waveguide intensity for 758-nm-thick α-MoO_3 is significantly the highest among the three thicknesses. Furthermore, by comparing the peak positions of TE_0 in Fig. 3(d) we observed that, as the thickness decreases, the peak of TE_0 shifts to the left, resulting in a decrease in the effective refractive index, consistent with the trend shown in Table S1.

In Fig. 3(d), the TE_0 mode was observed in all the Fourier transforms of the waveguide modes. To validate the experimental results, we adopted a three-layer model consisting of air, α-MoO_3 and SiO_2 to calculate the E_z distribution of the TE_0 mode by COMSOL. As shown in Fig. 3(e), we calculated the distribution of the propagation field of the TE_0 mode along the [100] direction at different thicknesses (758 nm, 300 nm and 180 nm). In Fig. 3(e), as the thickness increases, the electromagnetic fields dispersing in the substrate (SiO_2) diminish, which leads to stronger waveguide intensities in thicker α-MoO_3 flakes. This also confirms our results in Fig. 3(c), where the near-field intensity for 758 nm α-MoO_3 is significantly higher than that for α-MoO_3 with thicknesses of 300 nm and 180 nm. Additionally, the simulation results indicate that λ_m of the TE_0 mode decreases with increasing thickness. For comparison with experimental results, Fig. 3(f) exhibits the dependence of the TE_0 mode on thickness for both simulated and experimental data along the [100] direction. The red line represents the simulation results, while the blue squares are extracted from the experimental data. The close agreement between the experimental and simulated results indicates a negative correlation between thickness and wavelength.

The discussions above focus on waveguide modes along the [100] direction. However, α-MoO_3 flakes demonstrate in-plane anisotropy within the VIS and NIR ranges. Therefore, in addition to exciting waveguide modes along the [100] direction, waveguide modes can also be excited along the [001] direction, and the properties of waveguide modes for [100] and [001] directions should be different. In Fig. 4, we select an α-MoO_3 flake with a thickness of 248 nm to study the waveg-

uide modes along the [100] and [001] directions under incident light at 633 nm and 785 nm. The incident angle β is 45°. The AFM image of the 248-nm-thick α-MoO_3 is presented in Fig. S2. In Figs. 4(a) and 4(b), the near-field images display interference fringes parallel to the right boundaries, indicating that the waveguide modes of α-MoO_3 flakes can be excited by incident light at wavelengths of both 633 nm and 785 nm. The fringe period formed at 633 nm is shorter than that at 785 nm. The simulation results reveal that 248-nm-thick α-MoO_3 supports four waveguide modes, TE_0, TE_1, TM_0 and TM_1, along the [001] direction under 633 nm and 785 nm laser excitation. We performed Fourier transforms on the extracted fringe patterns to further explore the mode information carried by the fringes. As shown in Figs. 4(c) and 4(d), the α-MoO_3 flakes exhibit both TM_0 and TE_0 modes at a wavelength of 633 nm, whereas at 785 nm only the TE_0 mode is observed.

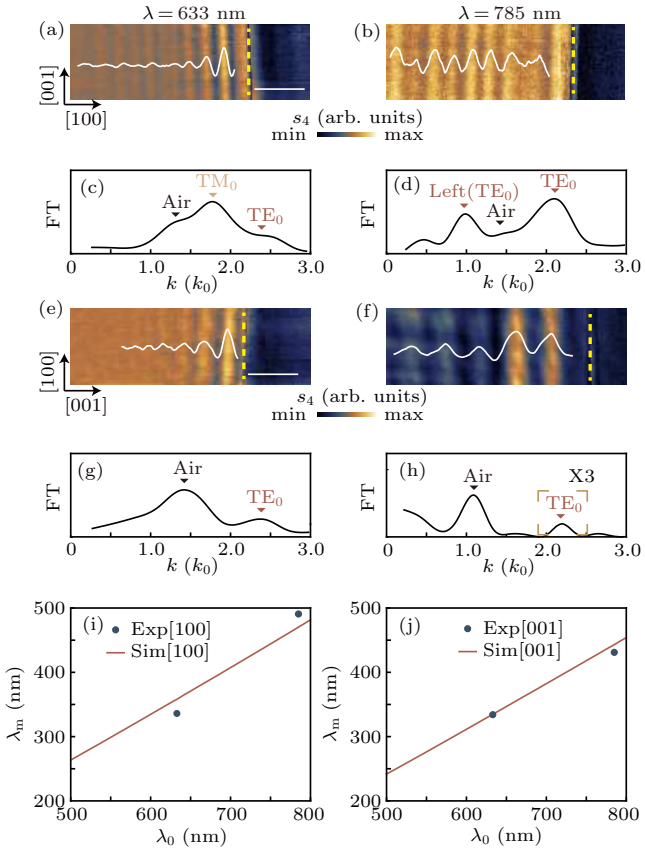


Fig. 4. Waveguide modes along the [100] and [001] directions on 248-nm-thick α-MoO_3 under different wavelengths of incident light at 45°. (a), (b) Near-field imaging of the α-MoO_3 flakes with $h = 248$ nm under 633 nm and 785 nm incident light at 45° for the [100] direction. The yellow dashed lines represent the right boundary of α-MoO_3 flakes. The scale bar is 1 μm. (c), (d) Fourier transform results of the near-field amplitude curves extracted along the [001] direction from (a) and (b). (e), (f) Near-field imaging of the α-MoO_3 flakes with $h = 248$ nm under 633 nm and 785 nm incident light at 45° for the [001] direction. The scale bar is 1 μm. (g), (h) Fourier transform results of the near-field amplitude curves extracted along the [001] direction from (e) and (f). (i), (j) Experimental and simulated TE_0 mode dispersion relation of the $h = 248$ nm α-MoO_3 flake along the [100] and [001] directions, respectively.

In Figs. 4(e) and 4(f), waveguide modes along the [001] direction were investigated by near-field imaging in 248-nm-thick α-MoO_3 flakes using 633 nm and 785 nm laser light at a 45° angle of incidence, which is the same equipment as used for analyzing the waveguide modes along the [100] direction. Comparing Figs. 4(e) and 4(f), the fringe period induced by 785 nm incident light is significantly larger than that induced by 633 nm light. Based on the Fourier transform results shown in Figs. 4(g) and 4(h), only a single TE_0 waveguide mode can be observed in 248-nm-thick α-MoO_3 along the [001] direction. Furthermore, unlike in the [100] direction, there are no interference fringes from the left boundary in the Fourier analysis along the [001] direction. This discrepancy is attributable to the rectangular shape of α-MoO_3, with the [001] direction aligned with its long axis, rendering interference fringes of the right boundary unaffected by those from the left boundary.

To quantitatively describe the in-plane anisotropy of the α-MoO_3 waveguide modes, the dispersion relations of the TE_0 mode along the [100] and [001] directions are plotted in Figs. 4(i) and 4(j). As shown in Figs. 4(i) and 4(j), the red lines respectively represent the simulation results for the [100] and [001] directions, while the blue circles correspond to the experimental results for the [100] and [001] directions, respectively. Overall, the experimental and simulated data show good agreement. The dispersion relationship demonstrates that λ_m of the TE_0 mode increases with the increase in the wavelength of the incident light. In-plane anisotropy is evident from the dispersion relation, where λ_m is longer in the [100] direction than in the [001] direction under the same incident light, signifying a larger effective refractive index along the [001] direction.

4. Conclusion and perspectives

In conclusion, our study on the near-field imaging of anisotropic waveguide modes along the [100] and [001] directions of α-MoO_3 flakes under VIS and NIR ranges (633 nm and 785 nm) significantly enriches our current understanding of the optical properties of α-MoO_3. This detailed investigation into the effects of thickness on the waveguide mode, along with the documentation of the dispersion relationship of the waveguides within the VIS and NIR range, paves the way for the innovative application of α-MoO_3 in full-spectrum optoelectronic devices. Our findings not only supplement the existing body of research on α-MoO_3 materials but also highlight the potential of α-MoO_3 as a versatile component in the development of next-generation optoelectronic devices owing to its in-plane optical anisotropy and lowloss waveguide capabilities. The in-plane anisotropy of materials facilitates the development of unique semiconductor devices for novel applications, including polarization-sensitive photodetectors, linearly polarized pulse generators and high-gain digital inverters.

Data availability statement

The data supporting this study's findings are available from the corresponding author upon reasonable request.

Acknowledgements

Project supported by the National Key Research and Development Program of China (Grant No. 2022YFA1203500), the Strategic Priority Research Program of the Chinese Academy of Sciences (Grant No. XDB30000000), and the CAS Youth Interdisciplinary Team.

References

[1] Zhang Q, Hu G, Ma W, Li P, Krasnok A, Hillenbrand R, Alù A and Qiu C W 2021 *Nature* **597** 187
[2] Liu Y, Huang Y and Duan X 2019 *Nature* **567** 323
[3] Li J, Yang X, Liu Y, Huang B, Wu R, Zhang Z, Zhao B, Ma H, Dang W, Wei Z, Wang K, Lin Z, Yan X, Sun M, Li B, Pan X, Luo J, Zhang G, Liu Y, Huang Y, Duan X and Duan X 2020 *Nature* **579** 368
[4] Hu D, Yang X, Li C, Liu R, Yao Z, Hu H, Corder S N G, Chen J, Sun Z, Liu M and Dai Q 2017 *Nat. Commun.* **8** 1
[5] Liang S, Cheng B, Cui X and Miao F 2020 *Adv. Mater.* **32** 1903800
[6] Wang H, Li Z, Li D, Chen P, Pi L, Zhou X and Zhai T 2021 *Adv. Funct. Mater.* **31** 2103106
[7] Wang R, Cui Q, Zhu W, Niu Y, Liu Z, Zhang L, Wu X, Chen S and Song L 2022 *Chin. Phys. B* **31** 096802
[8] Zhu D, Wang Z and Zhu D 2020 *J. Electron. Mater.* **49** 1765
[9] Wong D, Nuckolls K P, Oh M, Lian B, Xie Y, Jeon S, Watanabe K, Taniguchi T, Bernevig B A and Yazdani A 2020 *Nature* **582** 198
[10] Chen J, Badioli M, Alonso-González P, Thongrattanasiri S, Huth F, Osmond J, Spasenović M, Centeno A, Pesquera A, Godignon P, Zurutuza Elorza A, Camara N, De Abajo F J G, Hillenbrand R and Koppens F H L 2012 *Nature* **487** 77
[11] Falkovsky L A 2008 *J. Phys.: Conf. Ser.* **129** 012004
[12] Papageorgiou D G, Kinloch I A and Young R J 2017 *Prog. Mater Sci.* **90** 75
[13] Güler Ö and Bağcı N 2020 *J. Mater. Res. Technol.* **9** 6808
[14] Novoselov K S, Geim A K, Morozov S V, Jiang D, Zhang Y, Dubonos S V, Grigorieva I V and Firsov A A 2004 *Science* **306** 666
[15] Tiwari S K, Sahoo S, Wang N and Huczko A 2020 *J. Sci. Adv. Mater. Devices* **5** 10
[16] Yu W, Sisi L, Haiyan Y and Jie L 2020 *RSC Adv.* **10** 15328
[17] Huang H, Shi H, Das P, Qin J, Li Y, Wang X, Su F, Wen P, Li S, Lu P, Liu F, Li Y, Zhang Y, Wang Y, Wu Z and Cheng H 2020 *Adv. Funct. Mater.* **30** 1909035
[18] You R, Liu Y, Hao Y, Han D, Zhang Y and You Z 2020 *Adv. Mater.* **32** 1901981
[19] Dvorak M, Oswald W and Wu Z 2013 *Sci. Rep.* **3** 2289
[20] Zeng M, Liu J, Zhou L, Mendes R G, Dong Y, Zhang M Y, Cui Z H, Cai Z, Zhang Z, Zhu D, Yang T, Li X, Wang J, Zhao L, Chen G, Jiang H, Rümmeli M H, Zhou H and Fu L 2020 *Nat. Mater.* **19** 528
[21] Tang H L, Chiu M H, Tseng C C, Yang S H, Hou K J, Wei S Y, Huang J K, Lin Y F, Lien C H and Li L J 2017 *ACS Nano* **11** 12817
[22] Lu Q, Yu Y, Ma Q, Chen B and Zhang H 2016 *Adv. Mater.* **28** 1917
[23] Tian H, Tice J, Fei R, Tran V, Yan X, Yang L and Wang H 2016 *Nano Today* **11** 763
[24] Zhao S, Dong B, Wang H, Wang H, Zhang Y, Han Z V and Zhang H 2020 *Nanoscale Adv.* **2** 109
[25] Li L, Yu Y, Ye G J, Ge Q, Ou X, Wu H, Feng D, Chen X H and Zhang Y 2014 *Nat. Nanotechnol.* **9** 372
[26] Xia F, Wang H and Jia Y 2014 *Nat. Commun.* **5** 4458
[27] Yang Y, Liu S C, Li Z, Xue D J and Hu J S 2021 *Chem. Commun.* **57** 565
[28] Liu E, Fu Y, Wang Y, Feng Y, Liu H, Wan X, Zhou W, Wang B, Shao L, Ho C H, Huang Y S, Cao Z, Wang L, Li A, Zeng J, Song F, Wang X, Shi Y, Yuan H, Hwang H Y, Cui Y, Miao F and Xing D 2015 *Nat. Commun.* **6** 6991
[29] Lin J, Liang L, Ling X, Zhang S, Mao N, Zhang N, Sumpter B G, Meunier V, Tong L and Zhang J 2015 *J. Am. Chem. Soc.* **137** 15511
[30] Kim J S, Liu Y, Zhu W, Kim S, Wu D, Tao L, Dodabalapur A, Lai K and Akinwande D 2015 *Sci. Rep.* **5** 8989
[31] Ma W, Alonso-González P, Li S, Nikitin A Y, Yuan J, Martín-Sánchez J, Taboada-Gutiérrez J, Amenabar I, Li P, Vélez S, Tollan C, Dai Z, Zhang Y, Sriram S, Kalantar-Zadeh K, Lee S T, Hillenbrand R and Bao Q 2018 *Nature* **562** 557
[32] Zheng Z, Xu N, Oscurato S L, Tamagnone M and Chen H 2019 *Science Advances* **5** eaav8690
[33] Wen M, Chen X, Zheng Z, Deng S, Li Z, Wang W and Chen H 2021 *J. Phys. Chem. C* **125** 765
[34] Petronijevic E, Dereshgi S A, Larciprete M C, Centini M, Sibilia C and Aydin K 2022 *ACS Appl. Nano Mater.* **5** 5609
[35] Wu B Y, Shi Z X, Wu F, Wang M J and Wu X H 2022 *Chin. Phys. B* **31** 044101
[36] Dhanasankar M, Purushothaman K K and Muralidharan G 2010 *Solid State Sci.* **12** 246
[37] Zhang L, Wu G, Gu F and Zeng H 2015 *Sci. Rep.* **5** 17388
[38] Bortoti A A, Gavanski A D F, Velazquez Y R, Galli A and De Castro E G 2017 *J. Solid State Chem.* **252** 111
[39] Du Y, Li G, Peterson E W, Zhou J, Zhang X, Mu R, Dohnálek Z, Bowden M, Lyubinetsky I and Chambers S A 2016 *Nanoscale* **8** 3119
[40] Abedini Dereshgi S, Lee Y, Larciprete M C, Centini M, Dravid V P and Aydin K 2023 *Adv. Opt. Mater.* **11** 2202603
[41] Fang L, Shu Y, Wang A and Zhang T 2007 *J. Phys. Chem. C* **111** 2401
[42] Wong K P, Hu X, Lo T W, Guo X, Fung K H, Zhu Y and Lau S P 2021 *Advanced Optical Materials* **9** 2100294
[43] Mooshammer F, Chae S, Zhang S, Shao Y, Qiu S, Rajendran A, Sternbach A J, Rizzo D J, Zhu X, Schuck P J, Hone J C and Basov D N 2022 *ACS Photonics* **9** 443